Methods

Ab initio calculations

Atomic ordering of bcc Fe_2VAl was studied by Monte-Carlo simulations on the basis of the screened generalised perturbation method (SGPM) [1–3] with interactions obtained in the exact muffin-tin orbital coherent potential approximation (EMTO-CPA) [4,5].

Hamiltonian

The following configurational Hamiltonian has been used in statistical thermodynamics simulations

$$H = \frac{1}{2}\sum_{p}\sum_{\alpha,\beta\neq\delta} V_p^{(2)-\alpha\beta[\delta]} \sum_{i,j\in p} \delta c_i^{\alpha}\delta c_j^{\beta} + \frac{1}{3}\sum_{t}\sum_{\alpha,\beta,\gamma\neq\delta} V_t^{(3)-\alpha\beta\gamma[\delta]} \sum_{i,j,k} \delta c_i^{\alpha}\delta c_j^{\beta}\delta c_k^{\gamma} + h.o.t.. \quad (1)$$

Here, the summation is performed over different types of clusters (p and t stand for indices of the pairs and triangles), alloy components (designated by Greek letters) and lattice sites (i, j and k). $V_p^{(2)-\alpha\beta[\delta]}$ and $V_t^{(3)-\alpha\beta\gamma[\delta]}$ are the pair- and three-site effective interactions, which have been determined using the SGPM implemented in the Lyngby version of the EMTO-CPA code and $\delta c_i^{\alpha} = c_i^{\alpha} - c^{\alpha}$ is the concentration fluctuation of the α component from its average concentration c^{α} in the alloy at site i. The contribution from pair interactions in (1) can be reduced to a quasibinary form

$$H = -\frac{1}{2}\sum_{p}\sum_{\alpha\neq\beta} \tilde{V}_p^{(2)-\alpha\beta} \sum_{i,j\in p} \delta c_i^{\alpha}\delta c_j^{\beta}, \quad (2)$$

where $\tilde{V}_p^{(2)-\alpha\beta}$ are the usual binary effective interactions describing the mutual ordering of α and β atoms and are related to the multicomponent effective pair interactions $V_p^{(2)-\alpha\beta[\delta]}$.

Effective interactions calculations

In order to model the B2 and A2 order-disorder transitions, which both happen at high temperatures, the SGPM effective interactions have been calculated in a random $Fe_{0.5}V_{0.25}Al_{0.25}$ alloy using a lattice parameter of $a = 2.998$ Å, which roughly corresponds to the experimental one at the A2-B2 ordering transition. The one-electron excitations have been included using the Fermi-Dirac distribution function at 1500 K. Magnetic excitations of Fe and V atoms at 1500 K were modelled using the disordered local moment (DLM) model combined with a model, which takes into considerations longitudinal spin fluctuations (LSF). The DLM-LSF contribution to the entropy has been defined as

$$S_i^{\mathrm{lsf}} = d\ln(m_i), \quad (3)$$

where m_i is the local magnetic moment of the i-th component in the DLM-LSF state and the parameter d is element- and, in general, state-specific. In the case of V, $d = 3$, while in the case of Fe, $d = 2$ has been chosen for Fe in the random $Fe_{0.5}V_{0.25}Al_{0.25}$ alloy and $d = 1$ for Fe on the V-Al sublattice in the partially ordered B2-Fe(V, Al). Fe exhibits strong localised magnetic character on the V-Al sublattice in contrast to when being at its own sublattice, where it becomes a weak itinerant magnet.

The partially ordered B2-Fe(V, Al) alloy with composition $(Fe_{0.9}V_{0.05}Al_{0.05})(Fe_{0.1}V_{0.45}Al_{0.45})$ has also been used in SGPM effective cluster calculations due to the fact that V-Al effective interactions strongly renormalise in the partially ordered B2-alloy. Therefore, this effect should be taken into consideration to produce the correct B2−$L2_1$ ordering temperature.

Strain-induced contributions connected with local lattice relaxations caused by the atomic size mismatch of the alloy components are not included in the effective SGPM cluster interactions and would have to be obtained separately. Due to the complexity of the system, i.e. multiple alloy components and non-trivial magnetism, these contributions were neglected in the calculations, which led to an overestimation of the A2−B2 ordering transition.

Extended Data Fig.1a shows the effective pair interactions in the random bcc A2-alloy at 1500 K for the different pairs. The strongest interaction at the first coordination shell is given for the Fe-Al pair, which leads to the B2-type ordering at high temperatures and which drives the first A2−B2 phase transition. One can see that the nearest neighbour Fe-V interaction is rather weak, but also of the ordering type. There are also several strong three- and four-site interactions in this alloy, which affect the A2−B2 transition temperature, shifting it by about 200 K but which do not qualitatively change the picture of ordering. The A2−B2 ordering phase transition calculated from these interactions is about 2100 K in the Monte-Carlo simulations, which is about 600 K higher than the experimental one due to the previously mentioned neglected strain-induced interactions. If Monte-Carlo simulations were performed with the bcc effective interactions (obtained in the random bcc A2-alloy), the second B2−$L2_1$ ordering transition would be at 1160 K, which is lower than the experimental one that happens at 1350 K. However, Extended Data Fig.1b shows that the V-Al effective pair interactions are substantially renormalised at the V-Al sublattice where this transition happens such that the then calculated transition temperature is about 1330 K, which is only 20 K below the experimental one.

Electronic structure calculations

Electronic structure calculations of random and ordered Fe_2VAl alloys have been done using the coherent potential approximation (CPA) [6] and locally self-consistent Green's function (LSGF) technique [7,8], which accurately accounts for the local environment effects in random alloys. Both these techniques have been used within the EMTO method

referenced here as EMTO-CPA [9] and ELSGF [10], respectively. The EMTO-CPA calculations have been done with the Lyngby version of the Green's function EMTO code, where the screened Coulomb interactions were calculated in the single-site DFT-CPA [11] and SGPM. The EMTO-CPA method was used for calculating the density of states (DOS) of the infinitely dilute limit of antisite disorder ($x_{\mathrm{AS}} \to 0$) without taking into consideration the perturbation of the electronic structure of the nearest neighbor atoms. While the results for the $\mathrm{Fe_V}$ and $\mathrm{V_{Fe}}$ antisite defects are shown in the main article the $\mathrm{Fe_{Al}}$ defects show similar features (see Extended Data Fig.2), namely a magnetic ground-state solution as well as localised electronic states near the Fermi level E_{F}.

Furthermore, to confirm the effect of increasing the antisite defect concentration in $\mathrm{Fe_2VAl}$, supercells consisting of 108 atoms (54 Fe, 27 V, 27 Al) were created and the spin-polarised electronic structure was calculated using the Vienna Ab Initio Simulation Package (VASP) [12] as shown in Extended Data Fig.3. For the supercell calculations we used the standard general gradient approximation by Perdew, Burke, Ernzerhof (GGA-PBE) [13] for the exchange correlation term. After structural relaxation using a Γ-centered $3 \times 3 \times 3$ k-point mesh and a cutoff energy of 450 eV, we used a $5 \times 5 \times 5$ k-point mesh for the spin-polarised density of states calculations to attain high accuracy. Extended Data Figs.3a−c clearly show the occurence of sharp features in the energy-dependent DOS inside the gap near E_{F}, reminding of localised states. These states become broader upon inreasing the impurity concentration, eventually leading to the formation of new bands, which fill out the gap and turn the system more metallic-like. However, due to the periodic boundary conditions (Bloch's theorem) imposed on the system by the supercell approach the Anderson-localised nature of these states cannot be described by this method and will not reproduce the decoherence of the wave functions, i.e. their exponential decay. More advanced, cumbersome methods are required for predicting the correct delocalisation transition and electrical conductivity of such systems [14].

Charges

Hinterleitner et al. [15] recently calculated the charge transfer in the $\mathrm{Fe_2VAl}$ compound by means of Bader's quantum theory of atoms in molecules. Such Bader charge analysis of the charge transfer $\Delta q_{\mathrm{at}} = q_{\mathrm{at}}^{\mathrm{scf}} - q_{\mathrm{at}}^{\mathrm{sup}}$, with $q_{\mathrm{at}}^{\mathrm{scf}}$ and $q_{\mathrm{at}}^{\mathrm{sup}}$ being the self-consistently derived charge density and superposed atomic Bader charges respectively, showed that there occurs a significant charge transfer towards each Fe atom $\Delta q_{\mathrm{Fe}} = -0.75\,e$ from both V ($\Delta q_{\mathrm{V}} = 0.48\,e$) and Al ($\Delta q_{\mathrm{Al}} = 1.03\,e$) in $\mathrm{Fe_2VAl}$. To illustrate the localised nature of Fe antisite defects, we calculated the charge density and Bader charges for the above mentioned $3\times3\times3$ rhombohedral supercell (54 Fe, 27 V, 27 Al atoms) containing one Fe/V antisite exchange defect. We found that the calculated charge transfer of Fe antisite exchanges is almost neglibile (Fe/V defect: $-0.14\,e$ for Fe and V, Fe/Al defect: $-0.02\,e$ for Fe and $0.07\,e$ for Al). This clearly shows that the charge is more localised around these defects, which act as impurities that are isolated from the ordered $\mathrm{Fe_2VAl}$ host compound. Our calculations are also consistent with similar calculations of single $\mathrm{V_{Fe}}$ antisites by Bilc et al. [16].

Magnetic calculations

The magnetic moment of Fe antisites on the V and Al sublattice was calculated to about $2.2\,\mu_{\mathrm{B}}$ and $2.7\,\mu_{\mathrm{B}}$, respectively, while the magnetic moment of V on the Fe sublattice was calculated as $0.9\,\mu_{\mathrm{B}}$. We found that these results are very consistent in both the ferromagnetic and DLM calculations. Extended Data Fig.4 shows the calculated magnetisation from the Monte-Carlo-generated 1024 atoms supercells at high temperatures compared with the experimental saturation magnetisation. A remarkable agreement is found with respect to the experimental data supporting the Monte-Carlo-simulated degree of disorder in $\mathrm{Fe_2VAl}$ as well as the level of disorder in the quenched samples.

Experimental

Sample preparation

Highly pure bulk elements (Fe 99.99 %, V 99.93 %, Al 99.999 %) were stoichiometrically weighed and melted using a high-frequency induction heating technique. The ingots were melted several times to ensure homogeneity and the relative mass loss $\frac{\delta m}{m}$ after melting was extremely low ($< 0.04\,\%$) such that the polycrystalline samples could be considered of utmost stoichiometric quality. After melting the as-cast $\mathrm{Fe_2VAl}$ ingot ($m \approx 6\,\mathrm{g}$) was evacuated in a quartz tube at $\approx 10^{-5}$ mbar and annealed at 1123 K for 168 h, followed by furnace cooling. The ingot was then cut into five rectangular pieces ($m \approx 0.05 - 0.15\,\mathrm{g}$) using an aluminum oxide cutting wheel. Sample #1 was measured after furnace cooling (Labeled as 'Furnace cooled' in the article), while sample #2 − #5 were subjected to further heat-treatment at

$$\begin{aligned} \#2 &\to 1223\,\mathrm{K} \\ \#3 &\to 1323\,\mathrm{K} \\ \#4 &\to 1423\,\mathrm{K} \\ \#5 &\to 1523\,\mathrm{K} \end{aligned}$$

for 24 h, followed by rapid quenching in cold water (labeled as '950 °C, 1050 °C, 1150 °C, 1250 °C quenched' in the article). During this process the quartz ampoules containing the samples were backfilled with inert Ar to ensure thermal conductance to the cold water bath. In order to verify the reproducibility of the dramatic change in the thermoelectric response, we prepared a second batch of samples, synthesised in the exact same manner. We cut a rectangular piece of the as-cast ingot (labeled as 'As cast' in the article $\widehat{=}$ sample #0), which was then used for measurements and annealed the other remaining part of the ingot

at 1123 K for 168 h as for the first batch. Again, several pieces were cut from the ingot and subjected to further heat treatment at

$$\#6 \rightarrow 1073\,\mathrm{K}$$
$$\#7 \rightarrow 1653\,\mathrm{K}$$

for 24 h, followed by rapid quenching in water (labeled as '1000 °C, 1380 °C quenched' in the article). Due to the fact that the measured properties of these samples were perfectly consistent with the tendency of the other samples we concluded that our sample preparation set-up is consistent and reproducible.

Reproducibility & stability

Nonetheless, we further checked the reproducibility and consistency of our results by preparing an isoelectronic Fe_2VAl-based sample by slightly changing the composition to $Fe_2V_{0.95}Ta_{0.05}Al$. The results for the measured thermopower and power factor are shown in Extended Data Fig.5. One can see that an almost identical behaviour of the thermopower upon high-temperature quenching is found further validating the consistency and reproducibility of the temperature-induced disorder in this series of full-Heusler compounds.

Mechanical strength and stability are prerequisites for building reliable thermoelectric devices. Therefore, we tested the stability of the rapidly quenched sample by measuring the thermoelectric properties during several heating and cooling cycles. We find that the temperature-dependent thermopower and power factor (see Extended Data Fig.5a,b) are surprisingly stable and did not degrade during several measurement runs, in different directions of the sample, with several heating and cooling cycles, despite the rapid quenching procedure. This confirms that the temperature-induced disorder could be a valid strategy to optimise the performance of thermoelectric devices, at least when the operating temperature is sufficiently below the quenching temperature.

Sample characterisation

i) X-ray diffraction

We used high-resolution powder X-ray diffraction (XRD) to investigate the crystal structure. Samples were ground to a fine powder and probed with conventional Cu-Kα radiation in a Bragg-Brentano (θ, θ)-geometry using a PANalytical XPert Pro MPD at the X-Ray Center, TU Wien. The room temperature XRD patterns shown in Extended Data Fig.6a display no signs of any impurity phases and feature almost all peaks of the full-Heusler structure pattern although the (111) peak at $\approx 27^\circ$ is very weak in all samples (see Extended Data Fig.6b). This has been attributed to B2-type disorder induced by hand grinding and other cold work effects by Maier et al.[17] as well as by Van der Rest et al.[18] and is present in all samples. Unfortunately, this means that the evolution of increasing B2-disorder with increasing quenching temperature is hardly observable in XRD powder patterns. Furthermore, as has also been pointed out by Van der Rest et al.[18] previously the similar structure factors of Fe and V atoms make the observation of increasing D03 disorder almost impossible as well. Nonetheless, a slight weakening of the (200) peaks at $\approx 31^\circ$ as well as a slight peak broadening of the (422) peak at $\approx 82^\circ$ for the high-temperature quenched samples already hint towards increasing disorder. This is also corroborated by a slight increase of the lattice parameter a, which has been extracted by performing Rietveld refinements on the XRD patterns using the program PowderCell, from $a = 5.763 \pm 0.002$ Å, for the as-cast and furnace-cooled sample, to $a = 5.772 \pm 0.003$ Å, for the high temperature quenched samples. We want to emphasise that the metastable A2 structure (vanishing (111) and (200) peaks) occuring in Fe_2VAl above ≈ 1500 K, could not be stabilised during the quenching process, which has also been pointed out by Van der Rest[18]. This is probably due to the strong Fe-Al interactions that lead to a quick B2 ordering at high temperatures as indicated by our simulations. Summarising, the X-ray diffraction techniques present only minor qualitative evidence for the amount of disorder in Fe_2VAl samples. While neutron diffraction is better for differentiating Fe and V scattering factors, Rietveld refinements are tricky and often not unambiguous due to the large amount of possibilities for the site occupancies in this ternary system. Therefore, we chose a combination of advanced statistical thermodynamics calculations and detailed measurements of the magnetic properties to effectively track the disorder in high-temperature quenched Fe_2VAl.

ii) Microstructure and composition

We probed the microstructure of our samples with a scanning electron microscope (Quanta 250 FEG) using a backscattered electron (BSE) detector and checked the composition by means of energy dispersive X-ray (EDX) analysis. These measurements were performed at the University Service center for Transmission Electron Microscopy (USTEM). The SEM images displayed no signs of a secondary phase precipitation (see Extended Data Figs.6c−d) that could have led to the change in magnetic and transport properties shown in the main article. The chemical composition of the different samples was also identical within the error bar of EDX measurements, which allowed us to confirm that a change in the stoichiometry did not occur during heat treatment. Therefore, we conclude that the temperature-induced antisite disorder must have caused the dramatic changes in physical properties, presented in the main article.

Property measurements

i) DC magnetisation

Temperature- and field-dependent measurements of the DC magnetisation were carried out on a CRYOGENIC su-

per conducting quantum interference device (SQUID) in a temperature range from 3 K up to room temperature and field range from 0 up to 6 T. The isothermal magnetisation from 0 up to 6 T was measured at various temperatures. Extended Data Figs.7a−d show the isothermal magnetisation of furnace-cooled and 1050 °C-quenched Fe_2VAl as well as the corresponding Arrot plots M^2 vs B/M, which show a strong curvature toward the B/M-axis precluding a ferromagnetic order transition in these samples.

ii) Hall effect

The Hall resistance was measured with an in-house set-up using a He-cryostat and a 9 T superconducting magnet. The Van-der-Pauw method was used for spot-welding thin gold wires onto thin sample pieces with the appropriate geometry. The magnetic field was sweeped from −9 to 9 T at various temperatures from 4 K up to 300 K. For the as-cast and furnace-cooled samples, the anomalous contribution to the Hall effect was small and only relevant at low temperatures and low magnetic fields. We could thus easily extract the normal Hall coeffcient from the slope of the linear Hall resistance $R_0 = \frac{R_{xy}}{B}$ at higher fields where the anomalous contribution $4\pi R_S$ is saturated. The carrier concentration and carrier mobility of the dominant charge carrier were then evaluated by

$$\mu_H \equiv \frac{R_0}{R_{xx}} \tag{4}$$

and

$$n_H \equiv \frac{1}{e\,R_0}. \tag{5}$$

For the high-temperature-quenched sample, which showed an anomalous Hall effect (AHE) over the whole measured temperature range, we expect an influence of the AHE at higher temperatures.

One has to be aware that despite the linear Hall effect, there should exist both holes and electrons in this compound, which can make it difficult to interpret $n_H(T)$ and $\mu_H(T)$. However, at low temperatures, before $S(T)$ shows its pronounced maximum, the contribution from the dominant charge carrier should dominate the temperature-dependent behaviour. Extended Data Fig.9a shows the temperature-dependent Hall carrier concentration obtained from our Hall effect measurements. It can be seen that the furnace-cooled and as-cast sample display almost identical behaviour, which is also reflected in the transport measurements shown in the main article. The disordered 1250 °C-quenched sample on the other hand has a carrier concentration which is about an order of magnitude larger and comparable to that of ordered $Fe_2VAl_{0.9}Si_{0.1}$. As explained in the main article, this can be understood from delocalisation of charge carriers in the impurity band marked by the appearance of two mobility edges.

iii) Electrical resistivity

The electrical resistivity at low temperatures from 4 K to 300 K was measured in an in-house He-cryostate using a four-probe method with thin gold wires spot-welded onto the sample surface. Above room temperature the electrical resistivity was again measured by the four-probe method in a commercial set-up (ZEM3 by ADVANCE RIKO). The sample dimensions were measured with an approximate accuracy of 0.005−0.01 mm resulting in an error bar $\lesssim 2\,\%$.

iv) Thermopower

The thermopower at low temperatures from 4 K to 300 K was measured in an in-house set-up using a toggled heating technique to cancel out spurious voltages. Chromel-constantan thermocouples were used and soldered onto copper wires, which were spot-welded at the ends of the sample. The results, while in very good agreement with the high-temperature data, were adapted by a constant factor to match the measured data of the commercial set-up (ZEM3 by ADVANCE RIKO) at $T \approx 300$ K.

v) Thermal conductivity

The total thermal conductivity was measured by the laser flash method, which allows one to calculate the thermal diffusivity by measuring the time-dependent temperature signal. The specific heat was measured using a differential scanning calorimeter and the sample density was evaluated by making use of Archimedes' principle. The electronic contribution to the thermal conductivity was extracted from the Wiedemann-Franz law $\kappa_e/\sigma = L_0\,T$ by assuming a constant Lorenz number $L_0 \approx 2.44 \cdot 10^{-8}\,\mathrm{W\,\Omega\,K^{-2}}$. The thermal conductivity above room temperature for the as-cast and 1380 °C-quenched sample are shown in Extended Data Fig.9b. A multifold reduction of the phonon contribution κ_{ph} for the 1380 °C-quenched sample could be obtained. This can most likely be explained by the increased point defect scattering in the more disordered sample and further indicates drastic changes of not only the electronic but also the phononic structure due to the temperature-induced disorder. Additional studies on the beneficial effect of temperature-induced disorder to reduce the relatively large κ_{ph} in this compound might be worthwile to be pursued.

Charge transport model

The temperature-dependent electrical conductivity, thermopower and electronic thermal conductivity can be generally expressed as [19]

$$\sigma(T) = L_{11},\;\; S(T) = \frac{1}{T}\frac{L_{12}}{L_{11}},\;\; \kappa_e = \frac{1}{T}\frac{L_{11}L_{22} - L_{12}^2}{L_{11}}, \tag{6}$$

with L_{ij} being the electronic linear response coefficients, which are given by the Chester-Thellung-Kubo-Greenwood (CTKG) formulation [20] as

$$L_{11} = \int_{-\infty}^{\infty} \Sigma(E,T) \left(-\frac{\partial f(E,T)}{\partial E} \right) dE, \quad (7)$$

$$L_{12} = \frac{1}{|e|} \int_{-\infty}^{\infty} \Sigma(E,T)(E-\mu) \left(-\frac{\partial f(E,T)}{\partial E} \right) dE, \quad (8)$$

$$L_{22} = \frac{1}{e^2} \int_{-\infty}^{\infty} \Sigma(E,T)(E-\mu)^2 \left(-\frac{\partial f(E,T)}{\partial E} \right) dE. \quad (9)$$

Hereby, $\Sigma(E,T)$ denotes an energy-dependent transport function that depends on the physics of the system. It was shown that $\Sigma(E,T)$ near the mobility edge or more generally near the transport edge [21] of partly localised electronic systems, usually follows

$$\Sigma(E,T) = \Sigma_0(T) \left(\frac{E - E_c}{k_B T} \right)^s, \quad (10)$$

where $\Sigma_0(T)$ is an energy-independent prefactor, E_c is the critical energy for delocalisation, i.e. the mobility or transport edge and s is an exponent that determines the shape of the transport function and is usually material-dependent. For the Anderson transition the critical exponent s is between 0.5 and 2 depending on compensation and band hybridisation [22]. We extended this concept to impurity bands with two mobility edges (see Extended Data Fig.9a) and developed a model where the transport function increases following Eq.10 at the first mobility edge and decreases in the same manner at the second mobility edge. Thus, the total energy dependence of the transport function is given by its width W, height Σ_0 and exponent s (see Extended Data Fig.9a). By numerically evaluating the integrals in Eqs.7−9, we can model the temperature dependencies of the thermoelectric transport properties from such an impurity band. For normal parabolic bands with dominant acoustic phonon scattering the transport properties can be written as [23,24]

$$\sigma(T) = \sigma_0(T) F_0(\eta, T), \quad (11)$$

$$S(T) = \frac{k_B}{e} \left[\eta - \frac{F_1(\eta,T)}{F_0(\eta,T)} \right], \quad (12)$$

$$\kappa_e(T) = \frac{3F_0(\eta,T)F_2(\eta,T) - 4F_1^2(\eta,T)}{F_0^2(\eta,T)} \sigma(T) T, \quad (13)$$

where $\eta = \frac{E-\mu}{k_B T}$ is the reduced chemical potential and $F_j(\eta,T)$ represent the Fermi integrals [25]

$$F_j(\eta,T) = \int_0^{\infty} \frac{\xi^j}{1+\exp(\xi-\eta)} d\xi. \quad (14)$$

In contrary to σ and κ the thermopower does not depend on the absolute magnitude of the transport function, i.e. the transport height. The same is true for the parabolic band expression where one can see that $S(T)$ only depends on the Fermi integrals. The electrical conductivity on the other hand includes an energy-independent $\sigma_0(T)$, which does not cancel out and holds information about the band masses, band degeneracies and scattering mechanisms. Thus, when modelling temperature-dependent transport, one should start by modelling the thermopower, which is a more direct probe of the energy-dependent electronic structure and significantly reduces the number of model parameters [26]. We started by making a qualitative analysis and simulated the temperature-dependent thermopower with a simple parabolic two band model with a tiny band gap, where the Fermi level is positioned near the valence band edge. Such scenario is expected to be likely the case for the ordered Fe_2VAl compound [15,27]. We then introduced an impurity band near E_F and increased the width of its extended states, i.e. delocalised it. We already found a good qualitative agreement by just increasing the transport width (delocalisation), which gives the sign reversal of the thermopower over the whole temperature range without even shifting the Fermi level or adjusting the band masses. To further test the applicability of our model towards the measured data and make predictions for different doping concentrations, we developed a least-squares fit model. Extended Data Fig.9b shows the measured temperature-dependent thermopower from 4 K to 800 K together with least-squares fits from a simple two-parabolic band model as well as our extended model containing the impurity band. A remarkable agreement and improvement over the entire temperature range is found for the latter, while the former yields poor agreement at higher temperatures and unreasonable fitting parameters, which are not in agreement with our DFT calculations. The inset shows the predicted thermopower at room temperature as a function of the reduced chemical potential, predicting a sign reversal due to the delocalised impurity band, which was confirmed in our experiments. In order to calculate the thermoelectric figure of merit ZT, we used the very same parameters obtained from our thermopower modelling to evaluate the energy-independent prefactors of the electrical conductivity Σ_0, σ_0. We then calculated both σ and κ_e at 400 K as a function of η to obtain ZT as a function of η for a given value of κ_{ph}.

Data availability

The data that support the findings of this study are available from the corresponding author upon reasonable request.

Code availability

The computer codes that support the findings of this study are available from the corresponding author upon reasonable request.

[1] Ducastelle, F. & Gautier, F. Generalized perturbation theory in disordered transitional alloys: Applications to the calculation of ordering energies. *Journal of Physics F: Metal Physics* **6**, 2039 (1976).

[2] Ducastelle, F. Order and Phase Stability in Alloys (1991).

[3] Ruban, A. V., Shallcross, S., Simak, S. & Skriver, H. L. Atomic and magnetic configurational energetics by the generalized perturbation method. *Physical Review B* **70**, 125115 (2004).

[4] Andersen, O., Jepsen, O., Krier, G. & Kumar, V. Lectures on Methods of Electronic Structure Calculations. *World Scientific* **63**, 62–124 (1994).

[5] Vitos, L. *Computational Quantum Mechanics for Materials Engineers: The EMTO Method and Applications* (Springer Science & Business Media, 2007).

[6] Rowlands, D. A., Ernst, A., Györffy, B. & Staunton, J. B. Density functional theory for disordered alloys with short-range order: Systematic inclusion of charge-correlation effects. *Physical Review B* **73**, 165122 (2006).

[7] Abrikosov, I. *et al.* Order-N Green's function technique for local environment effects in alloys. *Physical Review Letters* **76**, 4203 (1996).

[8] Abrikosov, I., Simak, S., Johansson, B., Ruban, A. & Skriver, H. L. Locally self-consistent Green's function approach to the electronic structure problem. *Physical Review B* **56**, 9319 (1997).

[9] Vitos, L., Abrikosov, I. & Johansson, B. Anisotropic lattice distortions in random alloys from first-principles theory. *Physical Review Letters* **87**, 156401 (2001).

[10] Peil, O. E., Ruban, A. V. & Johansson, B. Self-consistent supercell approach to alloys with local environment effects. *Physical Review B* **85**, 165140 (2012).

[11] Ruban, A. V., Simak, S., Korzhavyi, P. A. & Skriver, H. L. Screened Coulomb interactions in metallic alloys. II. Screening beyond the single-site and atomic-sphere approximations. *Physical Review B* **66**, 024202 (2002).

[12] Kresse, G. & Furthmüller, J. Efficient iterative schemes for ab initio total-energy calculations using a plane-wave basis set. *Physical Review B* **54**, 11169 (1996).

[13] Perdew, J. P., Burke, K. & Ernzerhof, M. Generalized gradient approximation made simple. *Physical Review Letters* **77**, 3865 (1996).

[14] Dobrosavljević, V., Pastor, A. & Nikolić, B. K. Typical medium theory of Anderson localization: A local order parameter approach to strong-disorder effects. *EPL (Europhysics Letters)* **62**, 76 (2003).

[15] Hinterleitner, B. *et al.* The electronic pseudo band gap states and electronic transport of the full-Heusler compound Fe_2VAl. *Journal of Materials Chemistry C* **9**, 2073–2085 (2021).

[16] Bilc, D. I. & Ghosez, P. Electronic and thermoelectric properties of Fe_2VAl: the role of defects and disorder. *Physical Review B* **83**, 205204 (2011).

[17] Maier, S. *et al.* Order-disorder transitions in the Fe_2VAl Heusler alloy. *Acta Materialia* **121**, 126–136 (2016).

[18] Van der Rest, C., Schmitz, A. & Jacques, P. J. On the characterisation of antisite defects and ordering in off-stoichiometric Fe_2VAl-based Heusler compounds by X-ray anomalous diffraction. *Acta Materialia* **142**, 193–200 (2018).

[19] Yamamoto, K., Aharony, A., Entin-Wohlman, O. & Hatano, N. Thermoelectricity near Anderson localization transitions. *Physical Review B* **96**, 155201 (2017).

[20] Chester, G. & Thellung, A. The law of Wiedemann and Franz. *Proceedings of the Physical Society (1958-1967)* **77**, 1005 (1961).

[21] Kang, S. D. & Snyder, G. J. Charge-transport model for conducting polymers. *Nature Materials* **16**, 252–257 (2017).

[22] Carnio, E. G., Hine, N. D. & Römer, R. A. Resolution of the exponent puzzle for the Anderson transition in doped semiconductors. *Physical Review B* **99**, 081201 (2019).

[23] Kim, H.-S., Gibbs, Z. M., Tang, Y., Wang, H. & Snyder, G. J. Characterization of Lorenz number with Seebeck coefficient measurement. *APL Materials* **3**, 041506 (2015).

[24] May, A. F. & Snyder, G. J. Introduction to modeling thermoelectric transport at high temperatures. In *Materials, Preparation, and Characterization in Thermoelectrics*, 11–1 (CRC press, 2017).

[25] Kim, R., Wang, X. & Lundstrom, M. Notes on Fermi-Dirac integrals. *arXiv preprint arXiv:0811.0116* (2008).

[26] Garmroudi, F. *et al.* Boosting the thermoelectric performance of Fe_2VAl-type Heusler compounds by band engineering. *Physical Review B* **103**, 085202 (2021).

[27] Anand, S. *et al.* Thermoelectric transport of semiconductor full-Heusler VFe_2Al. *Journal of Materials Chemistry C* **8**, 10174–10184 (2020).

Acknowledgements Financial support for F.G., M.P., A.R., T.M. and E.B. came from the Japan Science and Technology Agency (JST), program MIRAI, JPMJMI19A1. Part of DFT simulations were performed on resources provided by the Swedish National Infrastructure for Computing (SNIC) at PDC (Stockholm) and NSC (Linköping) A.V.R. acknowledges a European Research Council grant, the VINNEX center Hero-m, financed by the Swedish Governmental Agency for Innovation Systems (VINNOVA), Swedish industry, and the Royal Institute of Technology (KTH). A.V.R. also gratefully acknowledges the financial support under the scope of the COMET program within the K2 Center "Integrated Computational Material, Process and Product Engineering (IC-MPPE)" (Project No 859480). This program is supported by the Austrian Federal Ministries for Climate Action, Environment, Energy, Mobility, Innovation and Technology (BMK) and for Digital and Economic Affairs (BMDW), represented by the Austrian research funding association (FFG), and the federal states of Styria, Upper Austria and Tyrol. Oleg Peil is thanked for comments on the manuscript.

Author contributions F.G., M.P. and A.R. conceptualised the experimental research. F.G., M.P. and A.P. planned the outline of the draft. F.G. supervised the measurements, collected the data and wrote the initial draft. A.V.R. performed the ab initio calculations. F.G. and A.R. developed the charge transport model. F.G., M.P., A.R., A.V.R., S.K., M.R., H.M., A.P., T.M. and E.B. discussed the results and modified the manuscript. M.K. contributed to the sample synthesis and measurements.

Competing interests The authors declare no competing interest.

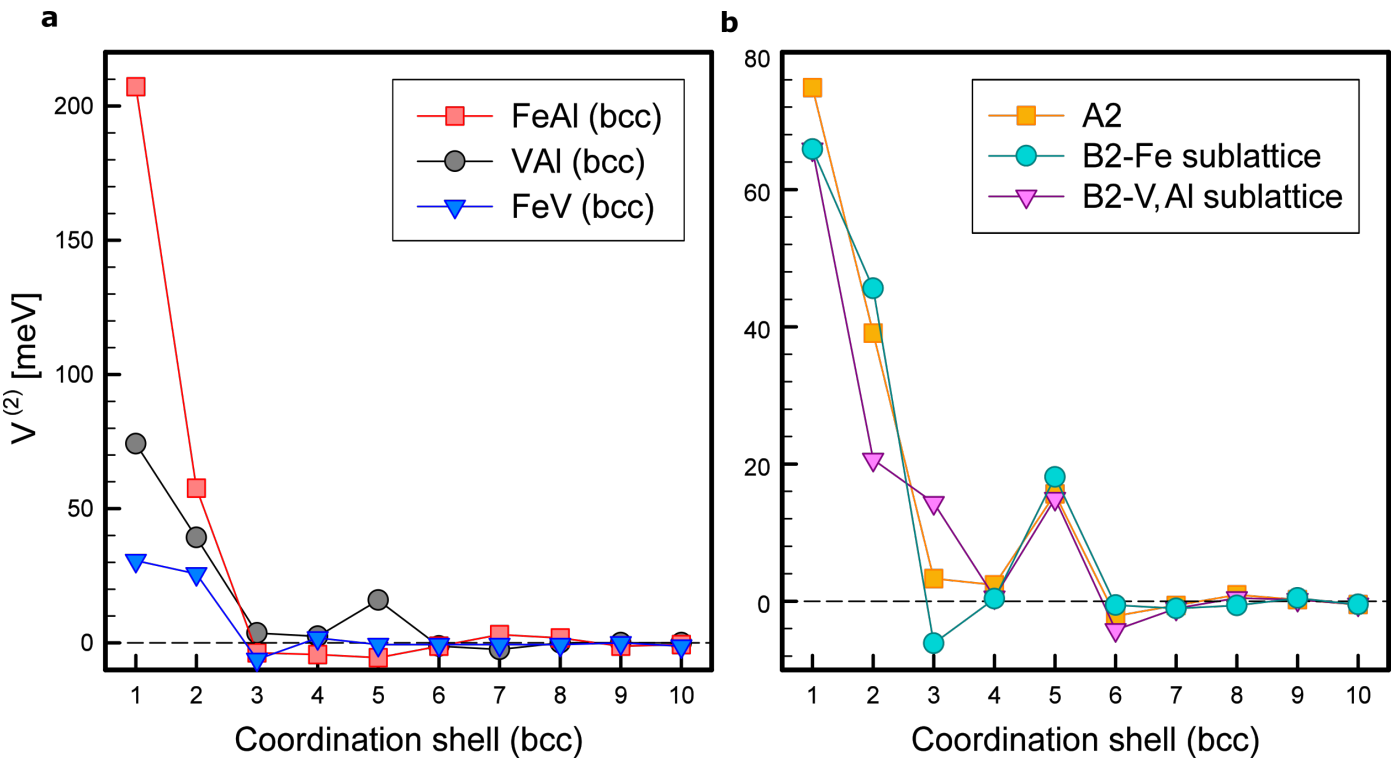

Extended Data Fig. 1: **a**, Calculated effective pair interactions in the bcc $Fe_{0.5}V_{0.25}Al_{0.25}$ alloy. **b**, V-Al effective pair interactions in the bcc $Fe_{0.5}V_{0.25}Al_{0.25}$ alloy and in the B_2 partially ordered alloy on the Fe and V – Al sublattices ·

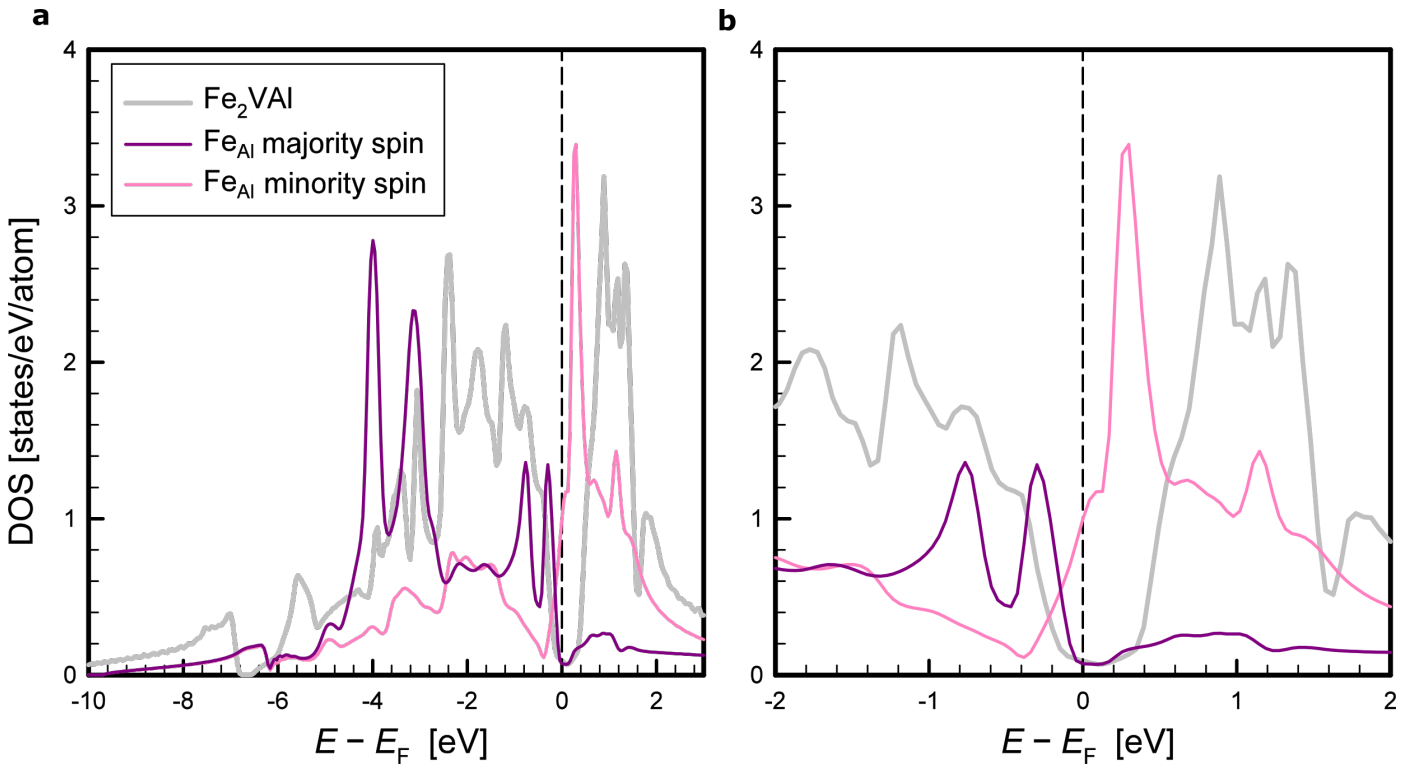

Extended Data Fig. 2: **a**, Spin-polarised density of states (DOS) of the single-impurity Fe_{Al} antisite defects compared to the DOS of pristine Fe_2VAl. **b**, Electronic states near the Fermi level E_F; calculated within the EMTO-CPA method.

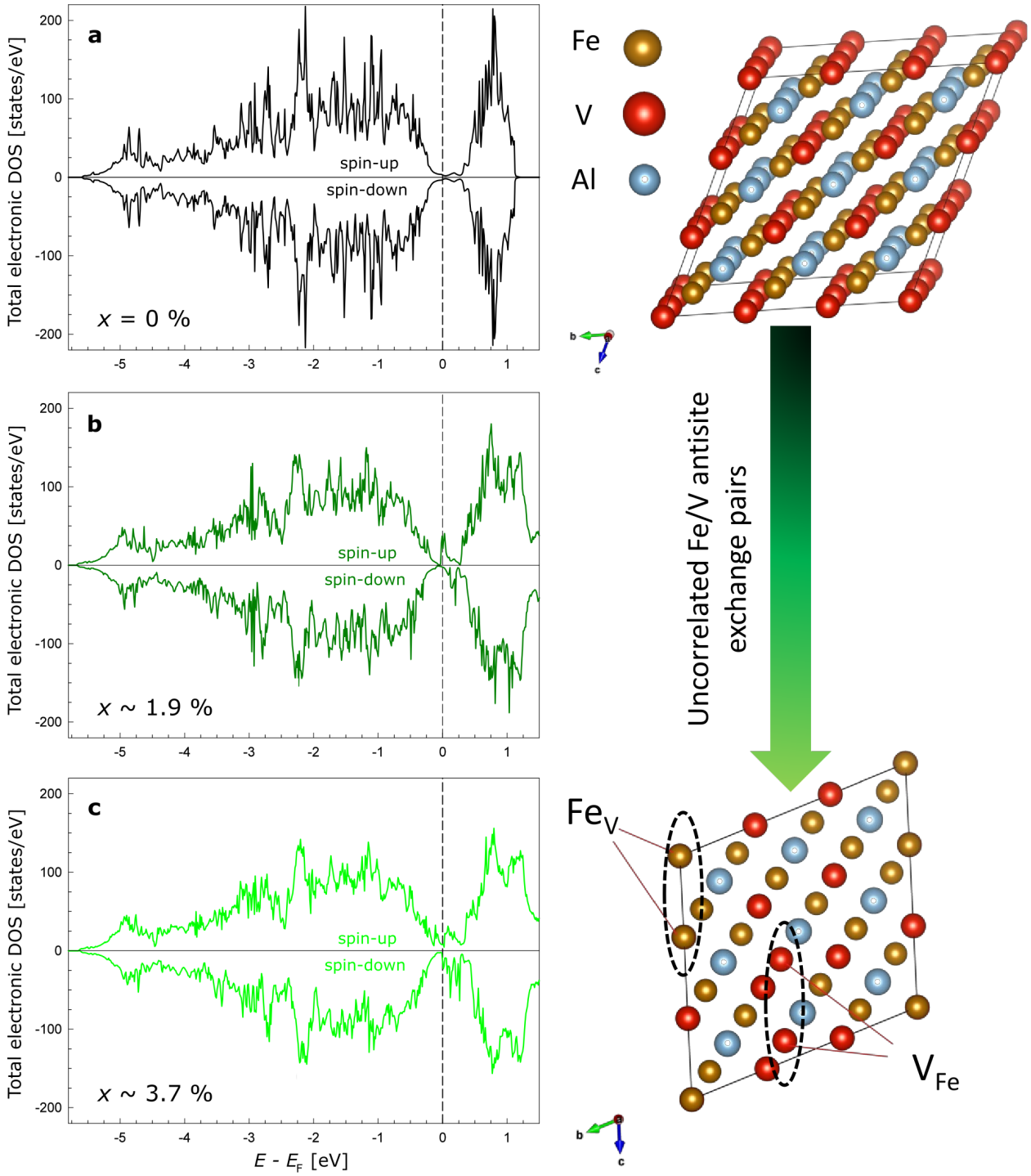

Extended Data Fig. 3: Total electronic density of states (DOS) for both spin channels of **a**, the pristine $3 \times 3 \times 3$ primitive supercell (108 atoms) of Fe_2VAl **b**, with one uncorrelated Fe/V antisite exchange defect (defect concentration: $x \approx 1.9\,\%$) and **c**, with two uncorrelated Fe/V antisite exchange defects ($x \approx 3.7\,\%$); Supercell electronic structure calculations were calculated in VASP using standard GGA-PBE functionals. A broadening of the localised in-gap states occurs when increasing the defect concentration. Sketch (right panel) shows the supercells used for the calculations.

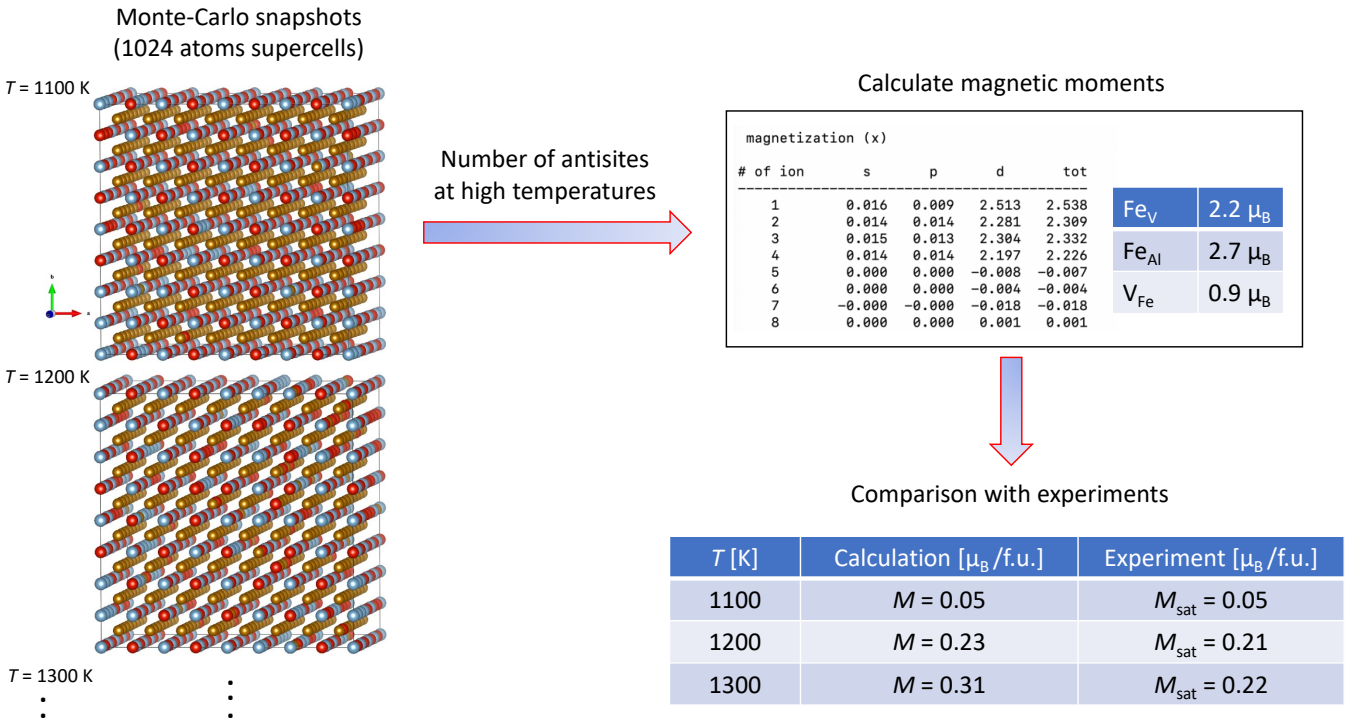

T [K]	Calculation [μ_B/f.u.]	Experiment [μ_B/f.u.]
1100	M = 0.05	M_{sat} = 0.05
1200	M = 0.23	M_{sat} = 0.21
1300	M = 0.31	M_{sat} = 0.22

Extended Data Fig. 4: Schematic of the procedure for calculating the magnetisation of high-temperature-disordered Fe_2VAl. 1024 atoms supercells were created from Monte-Carlo snapshots of high-temperature-disordered Fe_2VAl. The number of antisites were evaluated and their magnetic moments were calculated in VASP and compared with experimental data, yielding fairly good agreement.

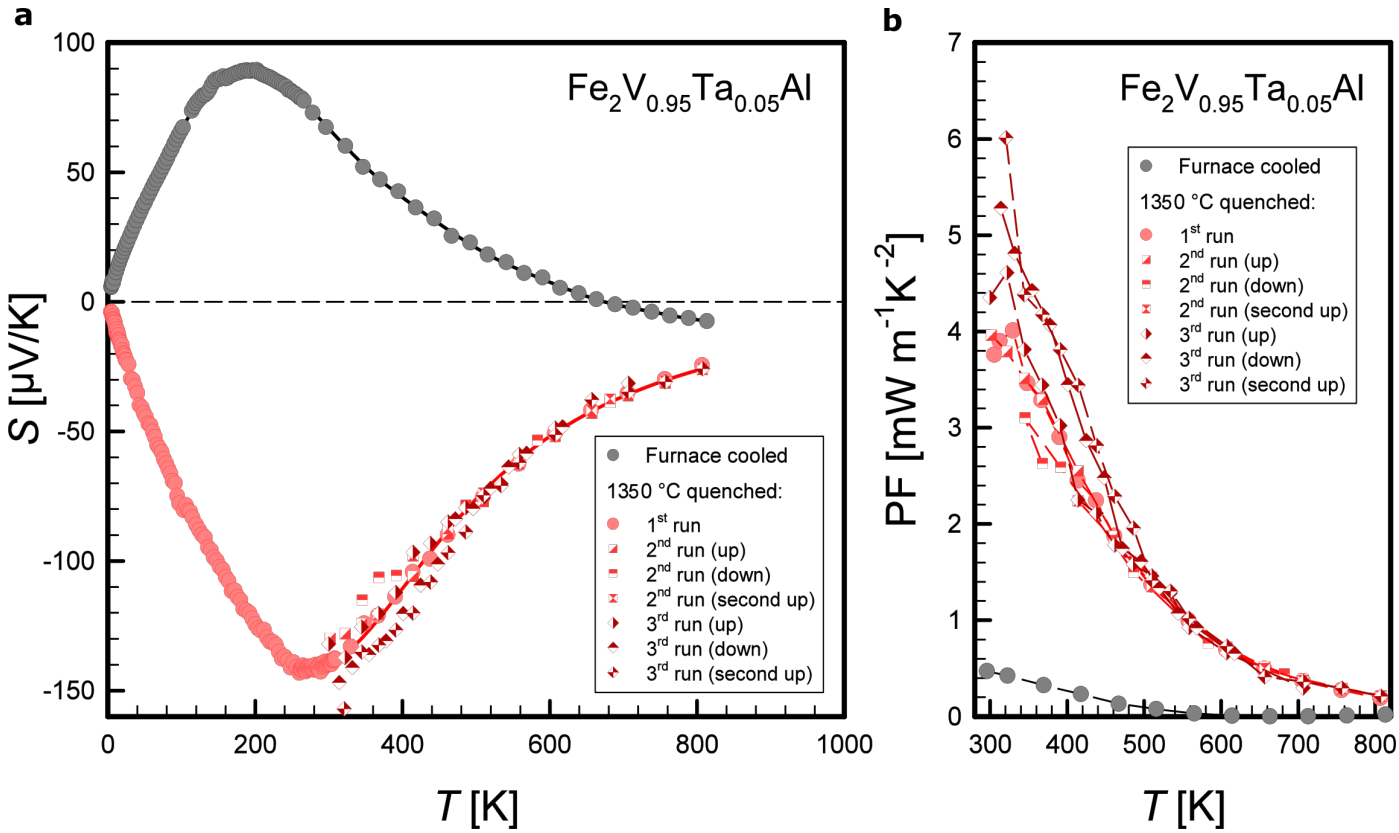

Extended Data Fig. 5: **a**, Measured thermopower of $Fe_2V_{0.95}Ta_{0.05}Al$, furnace cooled and quenched at 1350 °C. A sign reversal, similar to the one shown in the main article for Fe_2VAl, could be observed illustrating the reproducibility of this effect. Reasonably consistent results from various measurement runs above room temperatures with several heating and cooling cycles confirm a surprisingly good stability for the thermopower of the quenched sample. **b**, Power factor of $Fe_2V_{0.95}Ta_{0.05}Al$ from various measurement runs above room temperatures with several heating and cooling cycles.

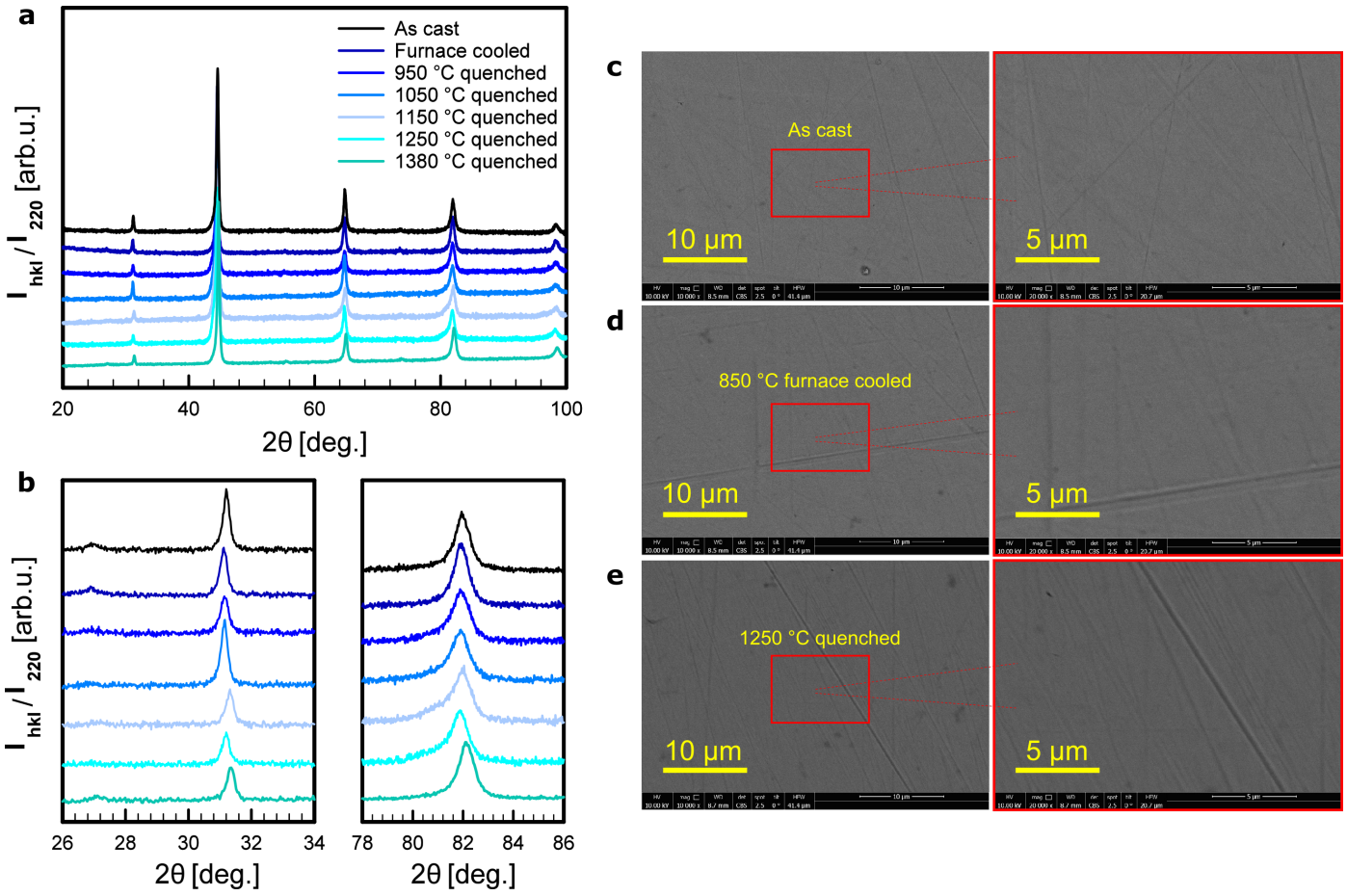

Extended Data Fig. 6: **a**, Normalised intensities of XRD powder patterns for Fe_2VAl samples analysed in this work. **b**, Magnificantions of the (111) peak at $\approx 27\,^\circ$ and (200) peak at $\approx 31\,^\circ$ in the left panel as well as the (422) peak at approximately $\approx 82\,^\circ$ in the right panel. **c**–**e**, Scanning electron microscopy images of a polished surface for as-cast, furnace-cooled and 1250 °C-quenched Fe_2VAl. Images were taken at different magnificantions using a back-scattered electron detector to search for potential impurity phase precipitation.

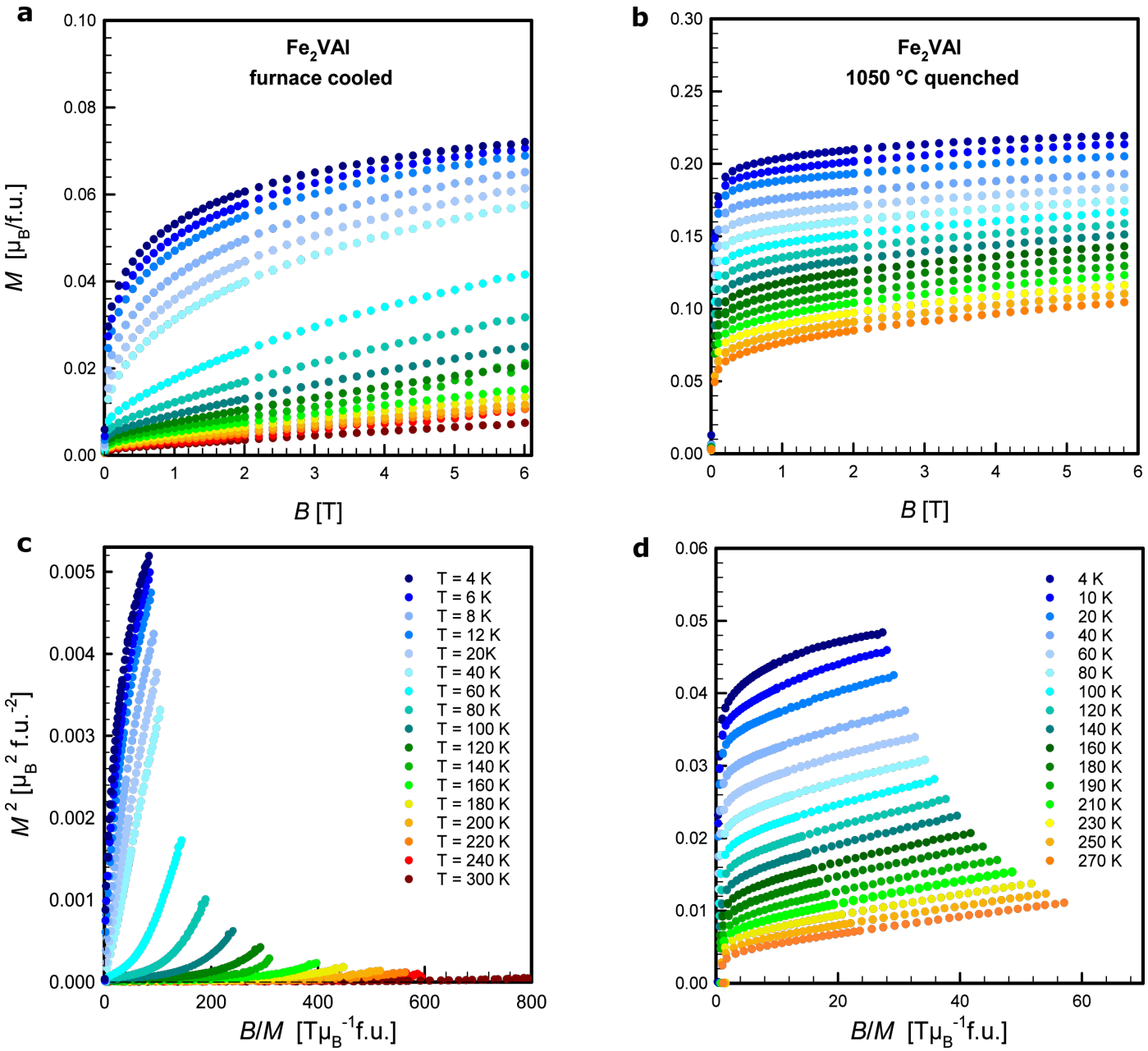

Extended Data Fig. 7: **a**,**b**, Isothermal, field-dependent magnetisation curves for furnace-cooled and 1050 °C-quenched Fe_2VAl, respectively. **c**,**d** Corresponding Arrot plots for furnace-cooled and 1050 °C-quenched Fe_2VAl.

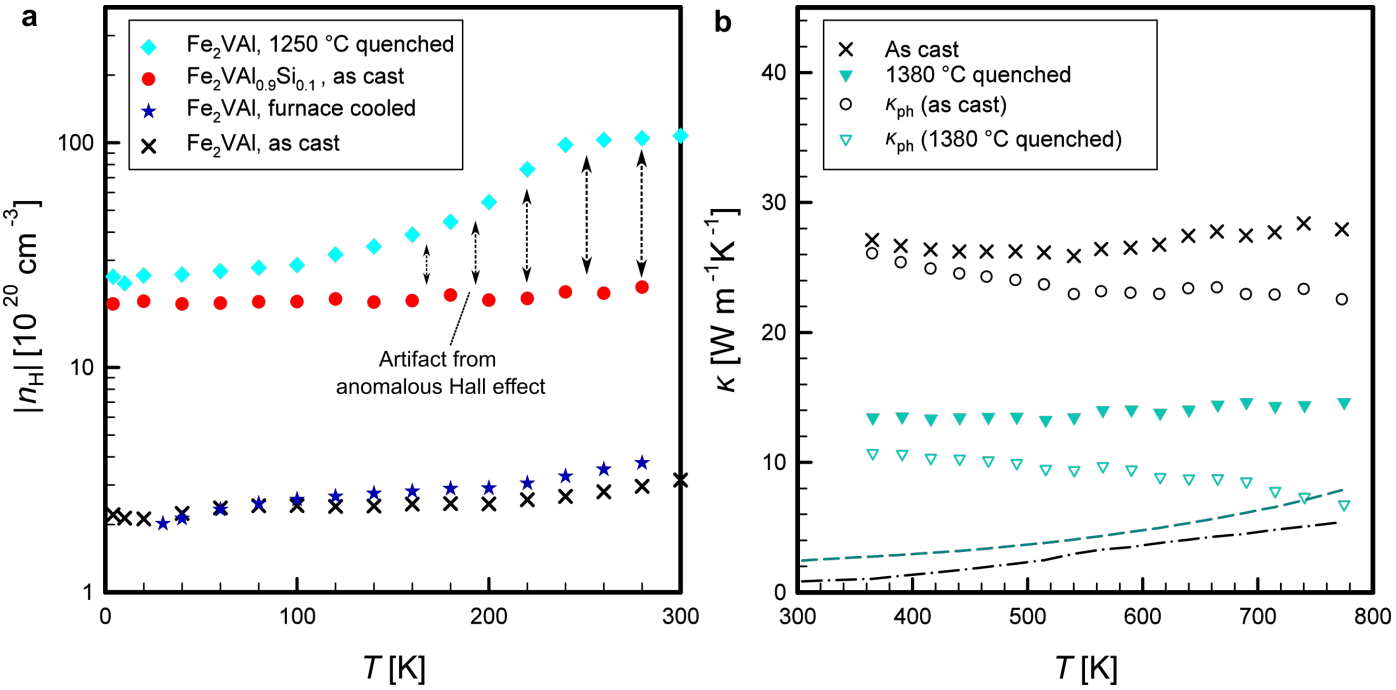

Extended Data Fig. 8: **a**, Absolute temperature-dependent Hall carrier concentration for as-cast, furnace-cooled and 1250 °C-quenched Fe_2VAl compared to as-cast $Fe_2VAl_{0.9}Si_{0.1}$. The increase of the evaluated carrier concentration above ≈ 100 K for 1250 °C-quenched Fe_2VAl is presumably a measurement artifact due to the anomalous Hall effect. **b**, Temperature-dependent thermal conductivity with electronic and phonon contributions of as-cast and 1380 °C-quenched Fe_2VAl. Dashed lines represent the electronic contribution κ_e.

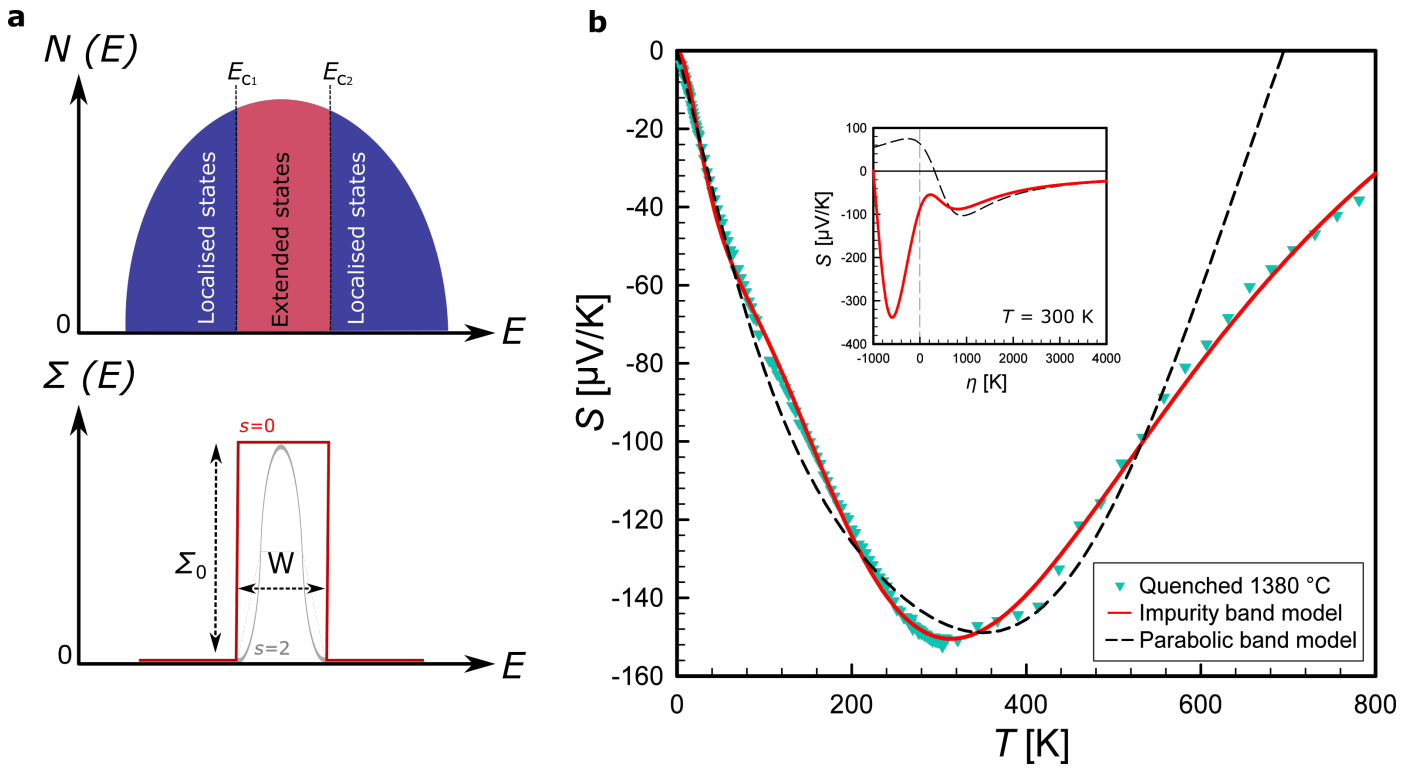

Extended Data Fig. 9: **a**, Schematic density of states $N(E)$ for the impurity band with Anderson-localised band tails and extended states in the center of the band. The width of the extended states is given by the mobility edges E_{c_1} and E_{c_2}. The energy-dependent transport function $\Sigma(E)$ with a transport width $W = |E_{c_2} - E_{c_1}|$ takes only finite values inside the extended states (i.e. within the delocalised regime). **b**, Temperature-dependent thermopower of 1380 °C-quenched Fe_2VAl from our experiments modelled with a parabolic two-band model and an enhanced model including the impurity band. The inset shows the predicted thermopower as a function of the reduced chemical potential, which gives a sign reversal due to the impurity contribution.